Sun *et al. Energy Mater.* **2025**, *5*, 500067
DOI: 10.20517/energymater.2024.228

Energy Materials

Article

Open Access

Check for updates

N/S co-doping design promising coal pitch derived carbon nanofibers toward advanced all-carbon potassium ion hybrid capacitors

Jinfeng Sun[1,#], Guangyuan Wang[1,#], Minyu Jia[1], Peng Yue[2], Yongfeng Ren[2], Hao Jiang[1], Yang Liu[1], Linrui Hou[1,*], Meng Chen[2], Changzhou Yuan[1,*]

[1]School of Materials Science & Engineering, University of Jinan, Jinan 250022, Shandong, China.
[2]Cospowers Technology Company Limited, Dongying 257000, Shandong, China.
[#]Authors contributed equally.

[*]**Correspondence to:** Prof. Linrui Hou and Prof. Changzhou Yuan, School of Materials Science & Engineering, University of Jinan, No. 336 Nanxinzhuang West Road, Shizhong District, Jinan 250022, Shandong, China. E-mail: mse_houlr@ujn.edu.cn; mse_yuancz@ujn.edu.cn

How to cite this article: Sun, J.; Wang, G.; Jia, M.; Yue, P.; Ren, Y.; Jiang, H.; Liu, Y.; Hou, L.; Chen, M.; Yuan, C. N/S co-doping design promising coal pitch derived carbon nanofibers toward advanced all-carbon potassium ion hybrid capacitors. *Energy Mater.* **2025**, *5*, 500067. https://dx.doi.org/10.20517/energymater.2024.228

Received: 29 Oct 2024 **First Decision:** 21 Nov 2024 **Revised:** 12 Dec 2024 **Accepted:** 17 Dec 2024 **Published:** 7 Mar 2025

Academic Editor: Hao Liu **Copy Editor:** Ping Zhang **Production Editor:** Ping Zhang

Abstract

Heteroatom-doped carbon materials have shown great potential as anodes for potassium ion hybrid capacitors (PIHCs) thanks to their diverse merits. However, their practicability is limited seriously by sluggish reaction kinetics, short cycling life, and low initial Coulombic efficiency, primarily because of the large ionic radius of K^+ and undesirable side reactions. Herein, the cost-efficiency low-softening-point coal pitch-derived one-dimensional N/S co-doped carbon nanofibers (N/S-CNFs) are smartly devised as competitive anodes for advanced PIHCs. The as-optimized N/S-CNF anode exhibits a compact morphology, abundant functional groups, and expanded interlayer spacing, rendering an improved initial Coulombic efficiency of 51.5%, high reversible capacities with 328.1 mAh g^{-1} at 0.1 A g^{-1} and 122.0 mAh g^{-1} at 5.0 A g^{-1}, and robust cycling stability. Theoretical calculations authenticate that N/S co-doping significantly enhances the electric conductivity and K^+ adsorption capability of fiber anodes. Detailed *in-situ* X-ray diffraction measurement unveils the intrinsic electrochemical K^+-storage process of N/S-CNFs. Moreover, the assembled PIHCs depict an extremely high energy density of 106 Wh kg^{-1} at 250 W kg^{-1}, and superb cycling performance with only 0.00016% capacity loss per cycle within 10,000 cycles, highlighting the superb practicality of our fabricated N/S-CNFs for next-generation PIHCs.

Keywords: N/S co-doped carbon nanofibers, low-softening-point coal pitch, initial Coulombic efficiency, high-rate anodes, potassium ion hybrid capacitors

INTRODUCTION

Metal ion hybrid capacitors (MIHCs) have attracted great attention thanks to their distinctive merits such as high energy density, excellent power density and superior cycling performance. MIHCs, generally composed of battery-type anodes and capacitive cathodes, combine both the merits of rechargeable batteries and supercapacitors[1]. So far, JM Energy has realized and mass-produced commercial lithium-ion hybrid capacitors (LIHCs), which have the potential for application in electric vehicles and portable electronics[2]. However, the scarce and unequally distributed lithium resources have greatly limited the sustainable development of Li^+-based electrochemical energy storage[3]. It will be a sustainable way to choose low-cost and widely distributed elements to replace the expensive lithium. In view of the abundant potassium resources and the low standard potential [-2.93 V *vs.* Standard Hydrogen Electrode (SHE)] which will provide high energy density, potassium ion hybrid capacitors (PIHCs) have great potential as alternatives for LIHCs[4]. In addition, since Al-K alloy is not formed, an Al foil can serve as the current collector for both the positive and negative electrodes of the PIHCs, greatly reducing the cost of devices[5]. However, compared with Li^+ (0.76 Å) and Na^+ (0.97 Å), K^+ with a larger ionic radius of 1.38 Å exhibits sluggish dynamics and severe volume expansion during charge-discharge cycles[6,7]. Thus, the mismatch of electrochemical kinetics and capacity between cathodic and anodic electrodes in PIHCs is more prominent[8]. It is critical to develop appealing anode materials for PIHCs with both high specific capacity and fast electrochemical kinetics.

To date, various anode materials of PIHCs have been extensively studied and reported, such as metal alloys[9], transition metal chalcogenides[10,11], phosphating compounds[12], metal oxides[13], MXene-based materials[14], and carbon materials[15,16]. Among them, coal pitch (CP)-derived soft carbon (SC) can obtain improved graphitization degree and enhanced electrical conductivity by adjusting the carbonization temperatures, thus delivering excellent rate performance[17-19]. However, the small interlayer distance of the SC always generates intense volume expansion during repeated K^+ ions insertion/de-insertion[20]. Taking graphite with an interlayer spacing of ~3.35 Å as an example, K^+ inserts into the graphite interlayer to form KC_8 during potassiation, causing a huge volume expansion of ~61%, which greatly hinders the rate performance and cycling stability[7]. So far, the main strategies for optimizing electrochemical K^+ storage kinetics of SC-based anodes include two aspects[21-23]: One is the nanostructure adjustment that ensures a short ion diffusion distance for rapid electron/ion transfer. Typically, compared with other dimensions[24], one-dimensional (1D) carbon nanofibers (CNFs) are promising anode candidates for PIHCs since the 1D nanostructure can provide convenient electrical conducting pathways for electrons and sufficient spaces for electrolytes and ions to transport and diffusion[25,26]. CP shows great advantages as a precursor to synthesize CNFs owing to the virtues of low cost, spinnability, and high carbon yield. Nevertheless, the low-softening-point (LSP) feature of CP (~80 °C) results in great difficulty in maintaining the fibrous structure during the carbonization process, which is still a huge challenge for fabrication of CP-based CNFs. Li *et al.* reported the electrospun CNFs from the mixture of polyacrylonitrile and coal liquefaction residues for both Li^+ and K^+ storage[25]. Zhang *et al.* constructed CNF-based films from LSP CP as free-standing anodes through a $Bi(NO_3)_3{\cdot}5H_2O$-assisted electrospinning-carbonization process[26]. In our previous work, LSP CP was pretreated with concentrated nitric acid to solve the softening problems of CP fibers during the pre-oxidation process[27]. Even so, the development of LSP CP-derived CNFs with superior K^+ storage properties remains a great challenge. The other effective approach is heteroatom doping (e.g., N, P, B, S and F)[28]. N is the most investigated doping element, which can provide abundant defects and additional active sites for K^+ ion adsorption, and enhance the conductivity. S, with a larger atomic size than C, could introduce more defects and expanded interlayer spacing for carbon materials[28-30]. S and N co-doping will

undoubtedly bring exceptional K^+ adsorption capacity and good rate performance meanwhile. The optimized carbon materials endowed with large specific surface area (SSA) and rich surface defects/functional groups could afford increased specific capacities, but they also lead to low initial Coulombic efficiency (ICE) attributed to the formation of solid electrolyte interphase (SEI) layers and decomposition of electrolyte during the first discharging[30,31]. Improving the capacity without losing the ICE simultaneously is still an enormous challenge.

Based on the above analysis, herein, a combined strategy, including the pre-oxidation, electrospinning, and followed sulfuration, was first developed to convert LSP CP to 1D N/S co-doped CNFs (N/S-CNFs). By pretreatment with HNO_3, the LSP CP was successfully electrospun with polystyrene (PS) to form nanofibers and maintained the fibrous morphology during pre-oxidation in air at 230 °C. By further sulfuration, the N/S-CNFs with abundant functional groups, expanded interlayer spacing, and reduced SSA were synthesized. Electrochemical results show that N/S-CNFs have impressive K^+ storage properties including high reversible K^+ storage capacities, excellent rate performance, improved ICE value and outstanding cycling performance. As a proof-of-concept application, a PIHC device constructed with a N/S-CNF anode achieves high energy density (106 Wh kg^{-1} at 250.0 W kg^{-1}), excellent rate performance and cycling stability.

EXPERIMENTAL

Synthesis of N/S-CNFs

To synthesize the precursor nanofibers, the LSP CP was pre-oxidation treated by a specific concentration of nitric acid for 12 h. After being thoroughly washed and dried, the pre-oxidized CP (2.4 g) was added into a mixed solution of 1.2 g PS in N, N-dimethylformamide (DMF) and N-methyl-2-pyrrolidone (NMP) (1:1 in volume ratio) and stirred overnight. Then, the obtained homogeneous solution was injected into a syringe and electrospun. An Al foil was placed at a distance of 20 cm from the needle to collect the spun fibers. The obtained fibers were dried at 60 °C and stabilized at 230 °C for 3h.

To synthesize N/S-CNFs, the stabilized fibers were blended with a proportionate sublimation sulfur and annealed at 600 °C, 700 °C, 800 °C, and 900 °C for 2 h in N_2 atmosphere at 5 °C min^{-1}. The obtained samples were named N/S-CNF-600, N/S-CNF-700, N/S-CNF-800 and N/S-CNF-900. For comparison, the sample obtained by annealing the stabilized CP/PS fibers at 700 °C without sulfur was denoted as CNF-700.

Synthesis of activated porous carbon nanofibers

To synthesize activated porous carbon nanofibers (aPCNF), the stabilized CP/PS fibers were thermally treated at 600 °C for 2 h at 5 °C min^{-1} with a N_2 protective atmosphere. The obtained sample was denoted as CNF-600. Then, CNF-600 was ground and mixed with 1.0 M KOH solution. The mass ratio of CNF-600:KOH was 1:3. After stirring for 24 h, the mixture was dried and then annealed at 900 °C for 3 h at Ar atmosphere. The material was carefully washed with 1.0 M HCl and deionized (DI) water until the pH reached 7.0, and then dried at 80 °C in a vacuum oven. The final product was denoted as aPCNF.

Materials characterizations

X-ray diffraction (XRD, Rigaku Ultima IV powder X-ray diffractometer with Cu Kα radiation, λ = 1.54056 Å) and Raman spectra (labRAM HR with an excitation wavelength of 532 nm) were conducted to characterize the phase structure of the samples. Morphologies and microstructures of products were analyzed with field-emission scanning electron microscopy (FESEM, JEOL-6300F operated at 6.0 kV and GeminiSEM 300 operated at 3.0 kV) and transmission electron microscopy (TEM, JEOL JEM 2100 Plus) with energy dispersive X-ray (EDX) spectroscopy. Micromeritics ASAP 2020 apparatus was selected to analyze the SSA and pore structure of samples. Fourier transform infrared (FT-IR) spectra were recorded using a Nicolet iS50 spectrometer with high purity KBr as reference. The composition and chemical valence

information of the samples were analyzed by X-ray photoelectron spectroscopy (XPS, Thermo ESCALAB 250Xi, Al Kα radiation).

Electrochemical measurements

70% N/S-CNFs, 20% conductive additives, and 10% polyvinylidene fluoride (PVDF) were thoroughly mixed in NMP to obtain a homogeneous slurry. The slurry was pasted onto an Al foil and then vacuum-dried at 80 °C for 12 h. Anode electrodes were obtained by cutting the dried foil into discs with a diameter of 12 mm and electroactive materials of ~1.2 mg cm^{-2}. Half cells were assembled using metallic K, glass fiber filter (Whatman GF/F), and 0.8 M KPF_6 in ethylene carbonate/dimethyl carbonate (1:1 in volume) as a counter/reference electrode, separator, and electrolyte, respectively. As for the cathode electrode, 10% PVDF, 20% acetylene black and 70% aPCNF were mixed with NMP, and pasted onto an Al foil. After vacuum-dried at 110 °C, the obtained aPCNF cathodes were constructed into half and full cells for electrochemical testing. To improve the stability of the N/S-CNF-700 anode in the first cycle and reduce the irreversible capacity, the pre-potassiation was conducted prior to the full cell assembly, during which the N/S-CNF-700 electrode was kept direct contact with metallic potassium under the additional pressure of the glass plate in the electrolyte. For charge balance, the weight ratio of cathodic and anodic electrodes is 3.5:1 with a total mass load of 3.6 - 4.5 mg per cell. Galvanostatic charge-discharge tests (GCD) were conducted using a battery testing system (Land CT2001A). Cyclic voltammetry (CV) and electrochemical impedance spectroscopy (EIS) were performed using an electrochemical workstation (Ivium).

The K^+ diffusion coefficient (D_{K+}) values were obtained based on[31]:

$$D_{K^+} = \frac{4}{\pi\tau} d^2 \left(\frac{\Delta E_s}{\Delta E_t}\right)^2 \left(\tau \ll \frac{L^2}{D_{K^+}}\right) \quad (1)$$

where d, ΔE_s and ΔE_t were the thickness of the film electrode, the potential change caused by discharge pulse, and the potential change caused by constant current discharge, respectively. Referenced from a previous study[32], the energy density (E, Wh kg^{-1}) and power density (P, W kg^{-1}) of PIHCs were calculated by:

$$P = \Delta V \times i/m \quad (2)$$

$$E = P \times t/3600 \quad (3)$$

$$\Delta V = (V_{max} + V_{min})/2 \quad (4)$$

where I was the discharge current (A), t was the discharge time (s), and m was the total mass of electroactive materials (kg). V_{max} and V_{min} were voltages at the beginning and end of discharge (V), respectively. The electrolyte stability window was related to the faradaic fraction S (*S value*) of PIHCs, which is calculated by[33]:

$$S = \frac{A_{pos}}{A_{neg}} - 1 \quad (5)$$

where A_{pos} and A_{neg} were the integral areas of the CV curve where the current was above and below 0 A, respectively.

First-principles calculation

All the calculations were conducted with the Vienna Ab Initio Simulation Package (VASP) based on Density Functional Theory (DFT). The exchange-correlation interaction and the core-valence electron interaction were modeled using Perdew-Burke-Ernzerhof (PBE) exchange function of the generalized gradient approximation (GGA) and the projector augmented wave (PAW) method, respectively. The cutoff energy was set as 400 eV, and the electronic energy threshold was 10^{-4} eV. For the geometrical optimization, the force convergence criterion on the atoms was lower than 0.05 eV $Å^{-1}$. The periodic 4 × 4 × 2 supercell was used to describe the carbon, N-doped carbon, and N/S-co-doped carbon surface. The irreducible Brillouin zone (IBZ) integration was sampled by 2 × 2 × 1 and 6 × 6 × 6 k-point meshes for the geometrical optimization and static computations.

RESULTS AND DISCUSSION

Microstructural characterizations

Typically, the overall synthesis of N/S-CNFs, as shown in Figure 1A, consists of three steps. Firstly, the LSP CP was treated with nitric acid, as reported in our previous contribution[27]. The CP/PS fibers were prepared by electrostatic spinning with the optimized ratio of LSP CP to PS. The obtained CP/PS fibers with smooth surface, high aspect ratio and uniform morphology are tightly entangled in random orientation [Supplementary Figure 1]. Then, the CP/PS fibers were stabilized by pre-oxidation at 230 °C in air and then carbonized with inert gases. After pyrolyzed at 700 °C, the fibrous morphology of CNF-700 [Figure 1B] with a porous surface and cracks also confirms that the pre-oxidation process effectively guarantees the fibrous structure of the samples. TEM observation [Figure 1C and D] further verifies the abundant pores and nanochannels located well in the disordered structure of the CNF-700.

Next, the sulfur doping is realized through the high-temperature annealing of the pre-oxidized fibers and sublimated sulfur mixture. As noted, when the temperature is above 115 °C, the sulfur will be liquefied and seeped into the pores of fibers under capillary action, where the pores are produced by pre-oxidation treatment and decomposition of PS at high temperatures. With increasing temperature, the fibers are carbonized, and sulfur atoms are introduced meanwhile into the carbon backbone by covalent bonding. At higher annealing temperatures, a large amount of sulfur sublimate, and simultaneously activate the carbon fiber matrix[34]. Notably, the as-obtained N/S-CNF samples all show a perfect morphology with fiber diameter mostly between 500 and 700 nm [Figure 1E and Supplementary Figure 2]. It is worth mentioning that after carbonization/sulfur doping, the surface of the fibers becomes even rougher and the cracks on the surface disappear accordingly. A TEM image [Figure 1F] assures the dense morphology of N/S-CNF-700 without any apparent pores or nanochannels. Similar observations are also evident in other N/S-CNF samples [Supplementary Figure 3], which may be attributed to the reaction between pyrolyzing carbon and S during high-temperature vulcanization causing the structural collapse and densification[31]. The compact 1D structure of N/S-CNFs will undoubtedly provide less electrode/electrolyte contact sur-/interfaces than that with porous channels, which is hugely beneficial for improving the ICE values[35].

A high-resolution (HR)-TEM image of N/S-CNF-700 [Figure 1G] evidences the carbon layer spacing of 0.381 nm, larger than 0.374 nm for CNF-700 [Figure 1D]. Undoubtedly, the increased interlayer spacing will be conducive to rapid insertion/de-insertion of potassium ions. Elemental Energy Dispersive X-ray Spectroscopy (EDS) mappings of the N/S-CNF sample visually confirm that C, S, N, and O elements are evenly distributed, revealing the successful introduction of N and S atoms into the carbon structure [Figure 1H and Supplementary Figure 4], while only C, N, and O species can be observed in CNF-700 [Supplementary Figure 5]. The elemental N in the fiber matrix should be derived from the pretreatment and pre-oxidation process by nitric acid. The S doping can enlarge the carbon layer spacing and provide additional active sites, while N doping favors increasing electrical conductivity, thus facilitating the K^+

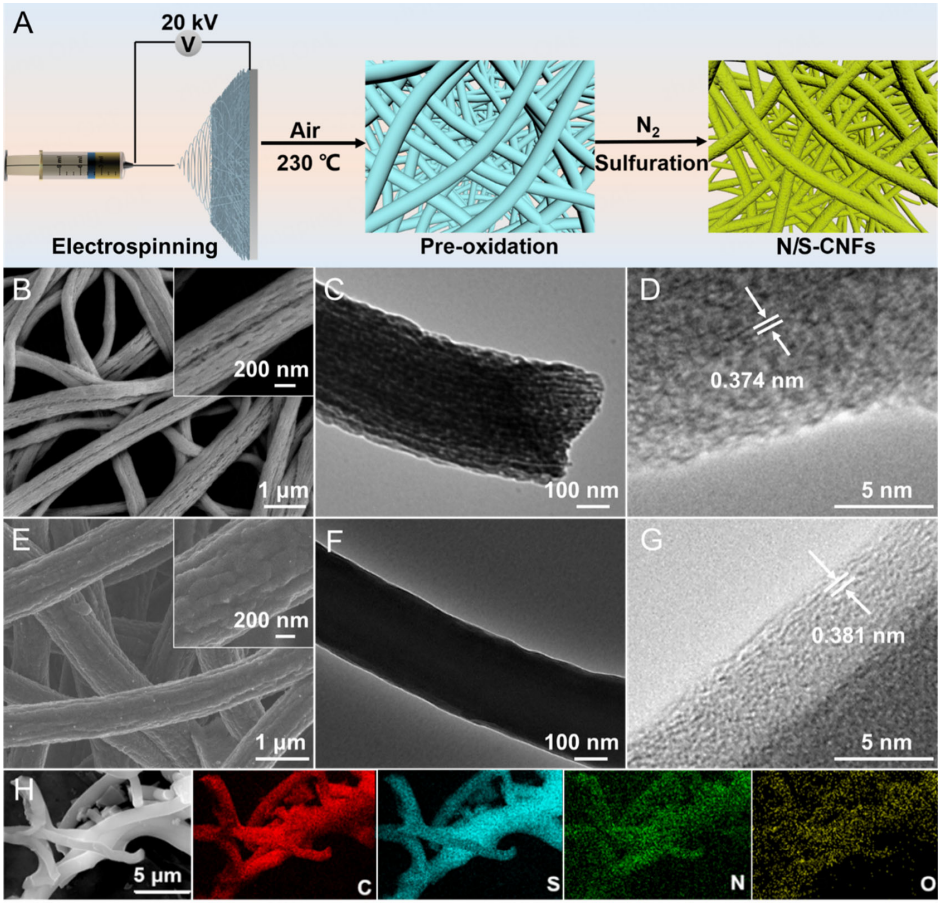

Figure 1. (A) Schematic for synthesizing N/S-CNFs; (B) FESEM; (C) TEM; and (D) HR-TEM images of CNF-700; (E) FESEM; (F) TEM; (G) HR-TEM; and (H) corresponding EDX elemental mapping images of N/S-CNF-700. N/S-CNFs: N/S co-doped carbon nanofibers; FESEM: field-emission scanning electron microscopy; TEM: transmission electron microscopy; HR-TEM: high-resolution (HR)-TEM; EDX: energy dispersive X-ray.

storage properties[34,36]. As vulcanization temperatures rise, the (002) interlayer spacing of N/S-CNFs shows a downward trend [Supplementary Figure 6], which may be attributed to the removal of a large portion of functional groups in the carbon matrix at high temperatures.

The structural characteristics of the N/S-CNFs were also evaluated using XRD and Raman characterization. All XRD patterns [Figure 2A] show two characteristic peaks at ~25.5° and 44 °, pointing to the (002) and (100) lattice planes of carbon materials, respectively[37]. Compared to that of CNF-700, the (002) reflection of N/S-CNF-700 becomes weaker and shifts slightly to a lower angle, indicating the increased defect degree and enlarged interlayer distance after sulfur doping. The (002) peaks of N/S-CNF-800 and N/S-CNF-900 both shift slightly to the lower angle and the diffraction peak at 44° strengthens, suggesting that high calcination temperatures increase the graphitization degree, which accords well with the HR-TEM observations. Raman spectra, as collected in Figure 2B, show broad D peaks (~1,349 cm^{-1}) related to the respiration effect of sp^2 carbon atoms in aromatic rings and G peaks (~1,570 cm^{-1}) derived from the conjugated structure of sp^2 carbon chains or rings[38]. As shown in the fitted atlas [Supplementary Figure 7], I band (~1,194 cm^{-1}) is assigned to impurities or heteroatoms, such as oxygen and sulfur atoms, on the graphite plane, and the D' band (~1,470 cm^{-1}) represents the defect in the graphene layer stack[39]. The intensity ratio of the D band and G band (I_D/I_G) values for CNF-700, N/S-CNF-600, N/S-CNF-700,

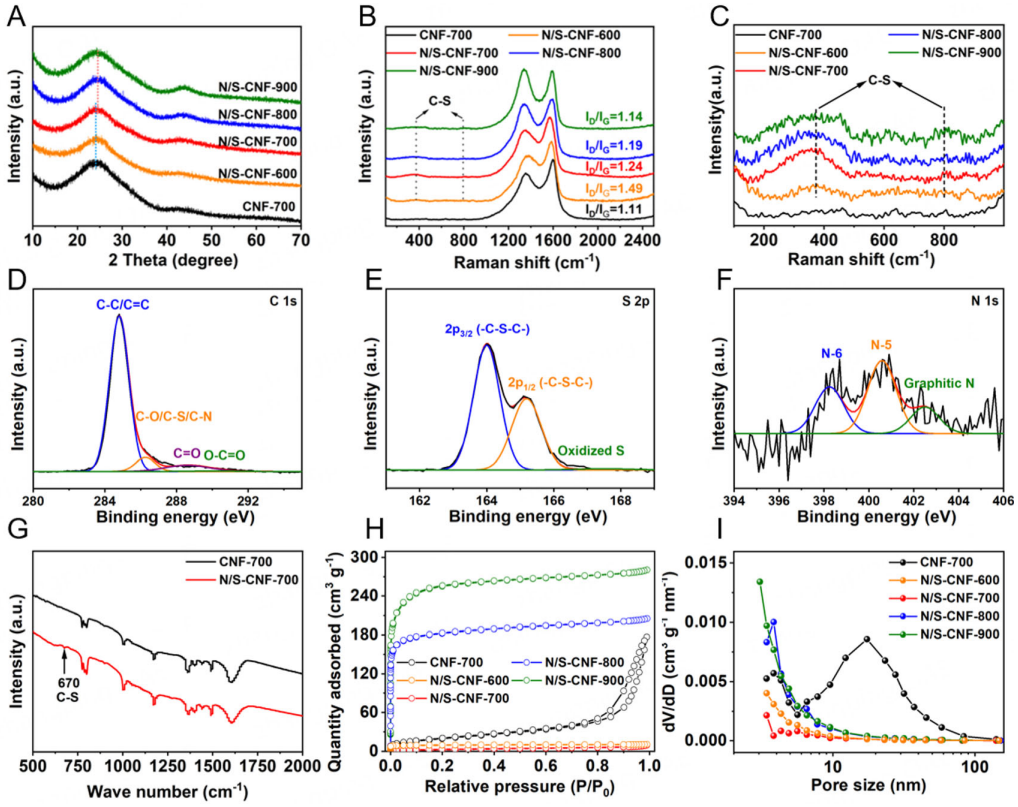

Figure 2. (A) XRD patterns; (B) Raman spectra; (C) enlarged view of the Raman region of N/S-CNFs; High-resolution XPS spectra of (D) C 1s; (E) S 2p and (F) N 1s for N/S-CNF-700; (G) FT-IR spectra of N/S-CNF-700 and CNF-700; (H) N_2 adsorption/desorption isotherms and (I) pore size distribution plots of N/S-CNFs and CNF-700 as indicated. XRD: X-ray diffraction; N/S-CNFs: N/S co-doped carbon nanofibers; XPS: X-ray photoelectron spectroscopy; FT-IR: fourier transform infrared.

N/S-CNF-800, and N/S-CNF-900 are 1.11, 1.49, 1.24, 1.19 and 1.14, respectively, revealing that the graphitization degree increases accordingly with elevated vulcanization temperature. Moreover, the G band of all S-CNFs shows a significant blue shift, which reaches the maximum offset (27.71 cm^{-1}) for N/S-CNF-700, highlighting the characteristics of n-type doping with improved conductivity[39]. Peaks at ~361 cm^{-1} and ~799 cm^{-1} can be observed in N/S-CNFS samples [Figure 2C], attributing to the stretching vibration and deformation of the C-S bond, which verified the successful doping of S species[31]. As a result, the S/N co-doping brings about abundant structural defects that may generate plenty of K^+ storage sites in CNFs.

Elemental composition analysis for CNF-700 and N/S-CNF-700 was conducted by XPS [Supplementary Figure 8]. Evidently, the elements of C (86.61 at.%), S (3.88 at.%), N (1.79 at.%), and O (7.72 at.%) co-exist in N/S-CNF-700, along with the C (91.58 at.%), N (2.85 at.%), and O (5.57 at.%) in CNF-700. C 1s spectra [Figure 2D and Supplementary Figure 9A] are divided into four peaks located at ~284.7 eV, ~286.1 eV, ~288.6 eV, and ~290.1 eV, corresponding to C-C/C=C, C-S/C-N/C-O, C=O, and O-C=O, respectively[21]. Three main peaks at 163.9 eV, 165.1 eV and 167.7 eV are indexed to S $2p_{3/2}$ (-C-S-C), S $2P_{1/2}$ (-C-S-C-), and the oxidized S group (-C-SO_x-C-) in S 2p spectra [Figure 2E][31,35]. The existence of S-based functional groups will lead to a significant increase in carbon layer spacing due to the even larger size of S than C atoms and provide abundant active sites[40]. The N 1s spectrum [Figure 2F and Supplementary Figure 9B] can be resolved into pyridinic N (N-6, 398.4 eV), pyrrolic N (N-5, 400.7 eV), and graphitic N (N-Q, 402.15 eV). Typically, N-Q is slightly electron-rich, which improves electronic conductivity of carbons and

facilitates charge transfer, while N-6 and N-5 located at edges of the carbon layers generate additional defects and active sites, which boost the K^+ storage properties[30,31]. Overall, N/S-CNF-700 with considerable functional groups could provide more defects and active sites, and expand the layer spacing, thus facilitating the storage and transportation of potassium ions[41]. Moreover, the FT-IR spectrum of N/S-CNF-700, compared to CNF-700 [Figure 2G], exhibits an additional peak at 670 cm^{-1}, which is attributed to the C-S bond tensile vibration, further validating the successful S doping[42].

N_2 adsorption/desorption curves for N/S-CNF samples are comparatively depicted in Figure 2H. Typically, CNF-700, N/S-CNF-600, and N/S-CNF-700 show type-I and type-IV combined isotherms, revealing their hierarchical porous structure[43], while N/S-CNF-800 and N/S-CNF-900 both present type-I isotherms, indicating the dominated micropores in both[20]. The SSA values of N/S-CNF-600 and 700 are estimated as 8.2 and 9.2 $m^2 g^{-1}$, respectively, greatly lower than that of CNF-700 (72.8 $m^2 g^{-1}$). Clearly, after S doping, the pores between 10 - 30 nm in pore size distribution curves [Figure 2I] almost disappear due to the structural collapse originating from the reaction of pyrolyzing carbon with the S during the high-temperature vulcanization[31]. Of particular note is that the SSA values for N/S-CNF-800 and N/S-CNF-900 are as high as 713.9 $m^2 g^{-1}$and 972.9 $m^2 g^{-1}$, respectively. This is primarily attributed to the generation of more pores from the rupture of the C-S bond at high temperatures, activated by sulfur molecules[44].

Electrochemical evaluation of the N/S-CNF anodes

The prepared samples were assembled into half cells for electrochemical tests to evaluate their K^+ storage properties. The first three CV cycles of the N/S-CNF-700 anode at 0.1 mV s^{-1} are shown in Supplementary Figure 10A. The sharp drop in peak at 1.0 V during the first scan can be attributed to the decomposition of the electrolyte, the formation of SEI films, and the irreversible capture of K^+ in the carbon matrix[35,45,46]. The reversible redox peak at 0.78/1.76 V in the following scans can be ascribed to the reversible adsorption/desorption of K^+ on the active sites[21]. Meanwhile, the following CV curves almost overlapped, showing excellent reversibility. In contrast, CNF-700 [Supplementary Figure 10B] does not show characteristic redox peaks. The effect of microstructure merits induced by sulfur doping on the K^+ storage properties is further manifested by the dQ/dV-V curves of N/S-CNF-700 and CNF-700 electrodes. As presented in Figure 3A, the dQ/dV-V profile of N/S-CNF-700 obtained from the 3rd charge-discharge cycle shows a couple of reversible peaks at 0.86/1.69 V, which belongs to the redox reaction between S-based functional group and K^+, corresponding to the redox peaks at 0.78/1.76 V in CV curves. While the CNF-700 electrode demonstrates no obvious redox peak, and the capacity contributed by each stage is much smaller than that of N/S-CNF-700. From the GCD plots of N/S-CNF-700 at 0.1 A g^{-1} [Figure 3B], the initial discharge/charge capacities of S-CNF-700 are 711.9/366.7 mAh g^{-1}, representing a high ICE of 51.5%, which is significantly higher than that of CNF-700 (27.1%, Supplementary Figure 11A) and previous reported carbon-based anodes [Supplementary Table 1]. This is reasonably attributed to the low SSA of N/S-CNF-700 and the significant role of the S groups in slowing down the SEI formation, which plays a critical role in the K^+ storage properties including ICE and cycling stability[47-49]. Thin and burly SEI could allow K^+ to pass through rapidly and block the transmission of electrons, while over-thick SEI will lead to high impedance of an electrode, affecting the transfer of K^+ ions[49]. Besides, N/S-CNF-600, N/S-CNF-800 and N/S-CNF-900 exhibit ICE values of 49.1%, 45.7% and 35.0%, respectively [Supplementary Figure 11B-D]. With the decrease in S content and SSA, the ICE values of N/S-CNFs show an impressive downward trend. More encouragingly, after the pre-potassiation treatment, the ICE of N/S-CNF-700 even can be increased to 93%, which is crucial for practical applications [Figure 3B].

The rate capability of N/S-CNFs was investigated at different current densities [Figure 3C]. Strikingly, the specific capacities of N/S-CNF-700 are 328.1 mAh g^{-1}, 296.1 mAh g^{-1}, 253.1 mAh g^{-1}, 209.5 mAh g^{-1}, 164.1 mAh g^{-1} and 122.0 mAh g^{-1}, corresponding to varying current densities of 0.1 A g^{-1}, 0.2 A g^{-1}, 0.5 A g^{-1},

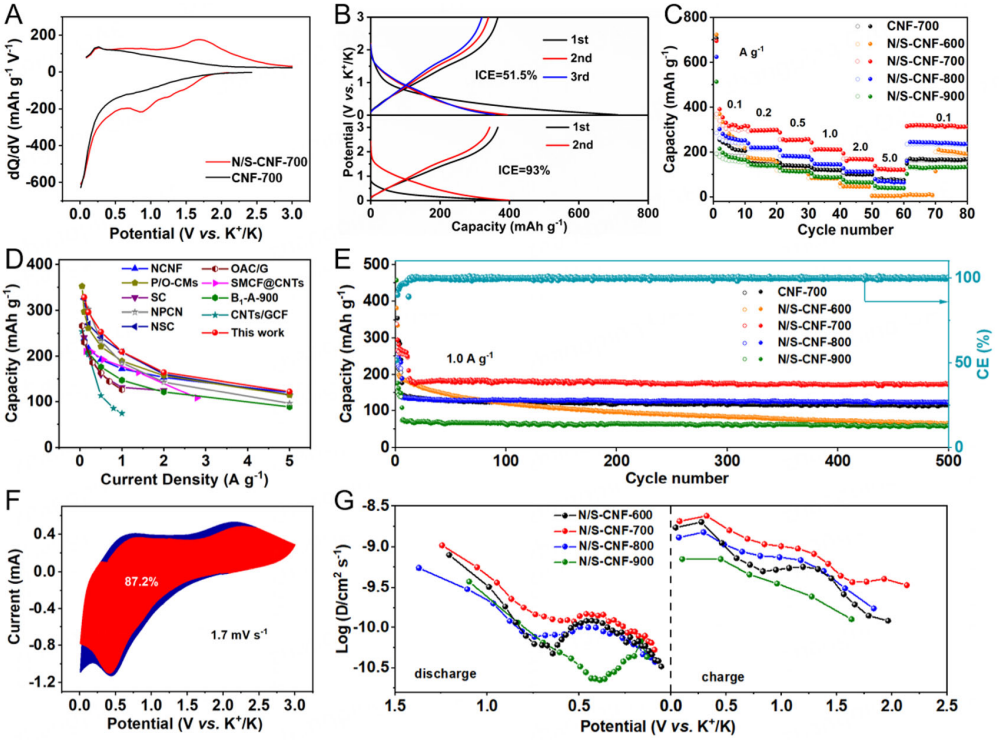

Figure 3. (A) Typical *dQ*/*dV* plots of N/S-CNF-700 and CNF-700 obtained from the 3rd charge-discharge cycle; (B) GCD plots before (the upper) and after pre-potassium (the lower) of N/S-CNF-700 at 0.1 A g^{-1}; (C) Rate capacities; (D) Rate capability of N/S-CNF-700 and comparison with latest reported carbon-based anodes[3,20,50-56]; (E) Cycling properties of N/S-CNFs anodes at 1.0 A g^{-1}; (F) CV curve (1.7 mV s^{-1}) with pseudo-capacitive contribution (red region) of N/S-CNF-700; (G) GITT profiles and corresponding D_{K+} values of N/S-CNF anodes over charge-discharge processes. N/S-CNFs: N/S co-doped carbon nanofibers; GCD: galvanostatic charge-discharge tests; CV: cyclic voltammetry; GITT: galvanostatic intermittent titration technique.

1.0 A g^{-1}, 2.0 A g^{-1} and 5.0 A g^{-1}, respectively, hugely higher than N/S-CNF-600 (280.5-4.3 mAh g^{-1}), N/S-CNF-800 (265.1-68.8 mAh g^{-1}), N/S-CNF-900 (182.3-40.6 mAh g^{-1}) and CNF-700 (253.6-73.6 mAh g^{-1}) at same current densities, confirming the superior structural merits of N/S-CNF-700 for efficient potassium storage particularly at high rates. As the rate is restored to 0.1 A g^{-1}, N/S-CNF-700 can restore to a high capacity of 256.4 mAh g^{-1}, further manifesting its good reversibility and stability. More competitively, the superb rate performance is much better than most of reported carbon anodes for K^+ storage, such as N-doped CNFs (NCNFs)[3], N/S dual-doped carbon nanosheets (NSC)[20], bituminous coals based carbon (B_1-A-900)[50], O-doped activated carbon/graphene composites (OAC/G)[51], carbon nanotube-modified graphitic carbon foam (CNTs/GCF)[52], P/O-enriched carbon microspheres (P/O-CMs)[53], waste-plastic-derived net-pocket-like carbon nanosheets (NPCN)[54], petroleum pitch-derived SC[55], and sub-micro carbon fibers wrapped in CNTs (SMCF@CNTs)[56], as summarized in Figure 3D. Figure 3E illustrates the cyclic properties of the N/S-CNF anodes at 1.0 A g^{-1}. After activation through the first few cycles, the charge/discharge curves of N/S-CNF-700 at a stable cycling process show similar shapes, as plotted in Supplementary Figure 12. The reversible capacity of N/S-CNF-700 still well remained as 174.9 mAh g^{-1} even after 500 cycles, significantly higher than other anodes including N/S-CNF-600 (64.3 mAh g^{-1}), N/S-CNF-800 (123.6 mAh g^{-1}), N/S-CNF-900 (59.8 mAh g^{-1}) and CNF-700 (116.5 mAh g^{-1}). Moreover, after 500 cycles, N/S-CNF-700 can maintain its 1D morphology, indicating its excellent structural stability [Supplementary Figure 13]. Similar results were obtained when the electrodes were tested at 0.1 A g^{-1} [Supplementary Figure 14]. As noted, the capacity of N/S-CNF-700 decreased slightly in the initial ten cycles, and then stabilized as 293 mAh g^{-1} after 100 cycles. By contrast, N/S-CNF-600, N/S-CNF-

800, N/S-CNF-900 and CNF-700 display relatively low reversible capacities of 113.1 mAh g^{-1}, 227.4 mAh g^{-1}, 150 mAh g^{-1} and 195.7 mAh g^{-1}, respectively, under the same cases. Such results further feature the optimal sulfur doping temperature of 700 °C, which renders additional absorption sites and expanded interlayer spacing, thus improving the potassium-storage capacities. One especially notes that the high ICE and cycling properties of the N/S-CNF-700 anode evidently surpass other reported carbon-based anodes [Supplementary Table 1].

For an in-depth understanding of the kinetic behaviors of N/S-CNF-700 anodes, the capacitive effect was qualitatively calculated from CV curves [Supplementary Figure 15A] using $i = av^b$, where a and b are constants[31]. A b value of 0.5 is typically characteristic of a diffusion-controlled process, while a b value of 1.0 stands for a characteristic surface-controlled process[31]. As derived from the log(i) versus log(v) curves, the b values of 0.98 and 0.86 were obtained for the oxidation and reduction peaks [Supplementary Figure 15B], revealing that the K^+ storage of N/S-CNF-700 anode comes from synergistic effect of diffusion- and surface-controlled processes[31]. The capacitive contributions at various scanning rates are distinguished based on $i = k_1v + k_2v^{1/2}$, where k_1v and $k_2v^{1/2}$ represent the current fractions from pseudocapacitive effect and diffusion-controlled part, respectively[57]. The pseudocapacitive contribution of N/S-CNF-700 at 1.7 mV s^{-1}, as profiled in Figure 3F, is calculated as high as 87.2%. Besides, the capacitive contribution increases with scan rates accordingly from 68.7% (0.2 mV s^{-1}) to an impressive value of 95.1% (2.2 mV s^{-1}), further manifesting that surface-controlled capacitive processes play a critical role in the charge storage of N/S-CNF-700 anodes [Supplementary Figure 15C][57]. This will favor the rate capability and cycling performance of anodes especially at high charge-discharge rates. In addition, the galvanostatic intermittent titration technique (GITT) was conducted at 0.1 A g^{-1} [Supplementary Figure 16] to calculate the D_{K+} of the N/S-CNF anodes. Evidently, N/S-CNF-700 shows D_{K+} values in the highest levels among the carbon anodes over the entire discharge-charge processes [Figure 3G][31,53]. Such high values of N/S-CNF-700 intrinsically reflect the fast K^+ diffusion, which is in favor of its excellent rate performance. EIS tests were also conducted to analyze the electrochemical process of the electrodes [Supplementary Figure 15D]. Compared with other N/S-CNFs, N/S-CNF-700 possesses the smallest semicircle diameter, indicating the smallest charge transfer resistance (R_{ct})[58]. Moreover, the slope of N/S-CNF-700 in the low-frequency region is obviously larger than other counterparts, further indicating the fastest ion diffusion in the electrode[59].

DFT calculations were managed to validate the advantages of introducing N/S into the carbon structure from the theoretical perspective. The geometries of the carbon, N-doped carbon, and N/S-co-doped carbon structures are optimized [Supplementary Figure 17]. The adsorption energy (ΔE_{ads}) of K^+ on the carbon was calculated by placing a single K at diverse sites in each model, and the most stable geometry structures can be obtained [Figure 4A-C]. The calculated ΔE_{ads} of N/S-co-doped carbon is -1.26 eV, remarkably lower than those of pure-phase carbon (0.05 eV) and N-doped carbon (-0.17 eV). The enhanced interfacial interaction between N/S-co-doped carbon and K^+ results in the most stable adsorption of K^+ ascribing to the synergistic doping of both N and S. The charge density difference plots [Figure 4D-F] show that there is stronger charge transfer between K and N/S co-doped carbon than others. Consumption of electronic charge around K ions and the accumulation of electronic charge around C atoms can be observed. The obvious charge transfer between the adsorbed K and N/S co-doped carbon can accelerate the diffusion and nucleation of K^+, which is consistent with the above experimental results. Careful examination of the total density of states [Figure 4G] of carbon, N-doped carbon, and N/S co-doped carbon reveals that the density of states of N-doped and N/S co-doped carbon cross over the Fermi level, manifesting the good electronic conductivity owing to the N-doping[60,61]. Overall, the doping of N and S can efficiently enhance interfacial interaction between carbon and K ions, which improves the adsorption and diffusion capability of K ions themselves.

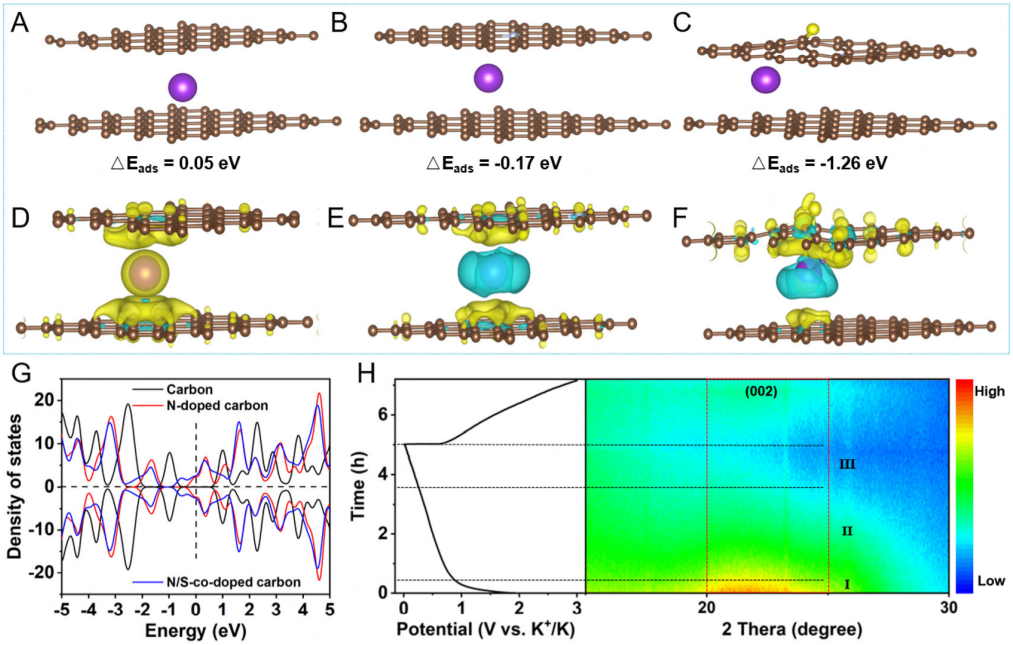

Figure 4. (A-C) Stable configurations and (D-F) charge density difference analysis of K^+ adsorbed on phase-pure carbon, N-doped carbon, and N/S co-doped carbon surface. K, C, S, and N are purple, brown, yellow and gray, respectively. And yellow and cyan contours with isosurface value of 0.001 e $Å^{-3}$ in panels indicate the accelerated and decreased charge density, respectively; (G) Density of states. Fermi level is set to 0 eV; (H) Voltage plots of N/S-CNF-700 during the first charging and discharging processes (0.1 A g^{-1}) and corresponding contour image of *in-situ* XRD peak intensities. N/S-CNFs: N/S co-doped carbon nanofibers; XRD: X-ray diffraction.

Moreover, to further understand the charge storage mechanism of K^+ in N/S-CNF-700, its structure evolution during the initial (de)potassiation process was monitored by an *in-situ* XRD test, as depicted in Figure 4H. The contour image shows that the (002) peak in the range of 20 - 25° of carbon material just changes in peak intensity, and no new peak and/or peak position shift can be found. According to the peak intensity change of (002), the discharge curve can be divided into three segments. In the interval (I), the peak intensity does not change greatly, which corresponds to the adsorption and storage of K^+ ions on the edge or surface defects of the carbon layer. The interval (II) is the redox reaction process of S-containing functional groups and K^+, in which the (002) peak is abated and carbon structure becomes chaotic. In the interval (III), as the reaction deepens, a large amount of K^+ is inserted into the carbon layer to form potassiation compounds (KC_x), and thus (002) peak disappears completely. Charging process can be identified as the inverse process of discharging. The disappeared (002) peak is gradually restored. Notably, the peak intensity is relatively weak compared with the initial state, which is due to the destruction of the carbon layer by insertion/de-insertion of potassium ions and the partially disordered transition of the carbon layer. This disordered transition adapts to the volume expansion results from K^+ ion insertion and de-insertion, consequently providing a stable structure for the following cycles[39].

Electrochemical performance of the N/S-CNF-700//aPCNF PIHCs

The attractive K^+ storage performance of N/S-CNF-700 including the high capacity, superior rate performance and excellent stability, as discussed above, makes it a great promising anode for PIHCs. Herein, aPCNF was used as the cathode to match with N/S-CNF-700 to construct the all-carbon PIHCs. The aPCNF possesses a stable capacity of 53.4 mAh g^{-1} at 1.0 A g^{-1} [Supplementary Figure 18]. Before assembling the full device, the N/S-CNF-700 electrode was pre-potassiated. To meet the charge balance of the two electrodes, the mass ratio of N/S-CNF-700 to aPCNF was fixed at 1.0:3.5. Considering the potential window of the involved N/S-CNF-700 and aPCNF electrodes and the *S*-value (i.e., Faraday fraction)[62], the

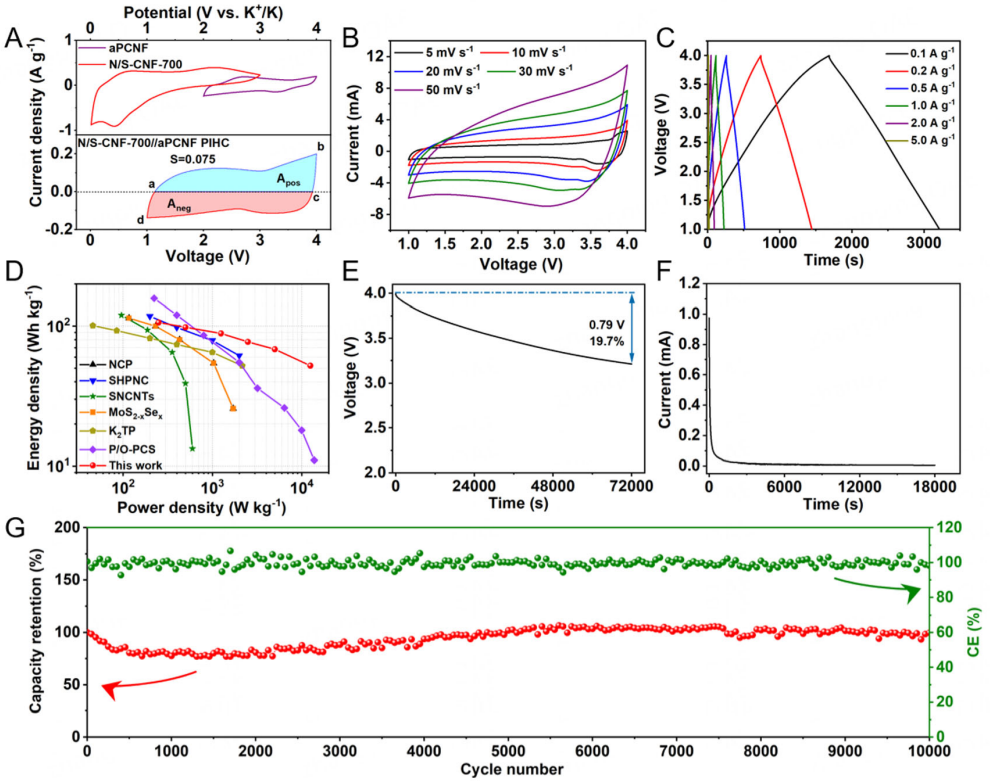

Figure 5. (A) CV curves of N/S-CNF-700, aPCNF, and N/S-CNF-700//aPCNF at 2 mV s^{-1}; Electrochemical properties of N/S-CNF-700//aPCNF device: (B) CV curves; (C) GCD profiles from 0.1 to 5.0 A g^{-1}; (D) Ragone plots compared with reported PIHCs[6,64-68]; (E) self-discharge; (F) leakage current; and (G) cycling stability at 1.0 A g^{-1}. CV: Cyclic voltammetry; N/S-CNFs: N/S co-doped carbon nanofibers; aPCNF: synthesize activated porous carbon nanofibers; GCD: galvanostatic charge-discharge tests; PIHCs: potassium ion hybrid capacitors.

upper and lower potential limits of the N/S-CNF-700//aPCNF cells are optimized as 4.0 V and 1.0 V, respectively, as plotted in Figure 5A. In general, the stable voltage window determination criterion is $S < 0.1$[63], and for our case here (scanning rate = 2 mV s^{-1}), the S value is estimated as ~0.075, which signifies the optimized electrochemical window of 1.0 V to 4.0 V for our assembled PIHCs.

Figure 5B shows the CV results of the assembled PIHCs at different sweep rates from 5.0 mV s^{-1} to 50.0 mV s^{-1}. Obviously, all CV curves depict slightly deviated rectangular shapes, reflecting the typical capacitive properties and good rate performance. Moreover, under various sweep rates, the S values are all < 0.1 [Supplementary Figure 19], further corroborating that the device can stably operate within such a voltage range. Meanwhile, GCD curves depict quasi-symmetric triangle shapes, further verifying the capacitive characteristic of the fabricated PIHC device [Figure 5C][6]. The reversible capacitances of 51.1 F g^{-1}, 50.5 F g^{-1}, 45.7 F g^{-1}, 39.7 F g^{-1}, 35.1 F g^{-1}, and 26.8 F g^{-1} are obtained corresponding to the current densities of 0.1 A g^{-1}, 0.2 A g^{-1}, 0.5 A g^{-1}, 1.0 A g^{-1}, 2.0 A g^{-1}, and 5.0 A g^{-1}, respectively [Supplementary Figure 20]. Ragone plots of the device are summarized in Figure 5D to further illustrate its superior energy and power density. Typically, at a power density of 250.0 W kg^{-1}, the device can obtain a high energy density of up to 106.0 Wh kg^{-1} and maintain a satisfactory energy density of 52.0 Wh kg^{-1} even at an extremely high power density of 1.25 kW kg^{-1}. Also, compared with other reported PIHC devices[6,64-68], the N/S-CNF-700//aPCNF device shows much superior electrochemical performance [Figure 5D]. Self-discharge properties of the N/S-CNF-700//aPCNF device were also tested, as shown in Figure 5E. Obviously, after being fully charged to 4.0 V at 0.1 A g^{-1}, the open-circuit voltage of the device decreased by 0.79 V after 20 h,

corresponding to a voltage loss of about 19.7%. In addition, the leakage current of the cell is only 6 μA [Figure 5F]. The N/S-CNF-700//aPCNF device with extremely low self-discharge properties could allow for effective charge storage and remarkable cycling stability[69]. As shown in Figure 5G, clearly, after 10,000 consecutive charging and discharging tests at a current density of 1.0 A g^{-1}, the capacitance retention is estimated to be 98.4% (i.e., ~0.00016% capacity loss per cycle). Moreover, a high Coulombic efficiency (CE) of approximately 100% was obtained during the whole test, further demonstrating the superb long-duration cycling characteristics. The outstanding electrochemical performance of N/S-CNF-700 promises its broad practical value and bright application prospects.

CONCLUSIONS

In conclusion, a heteroatom co-doping strategy was smartly explored in this work to achieve high-performance CNFs as advanced anodes with high ICE and superior rate behaviors toward PIHCs. The HNO_3 pretreated LSP CP was purposefully electrospun into fibers. With further pre-oxidization and calcination with sublimation sulfur, the 1D N/S-CNFs, to the best of our knowledge, were obtained for the first time using the low-cost LSP CP. With the rational regulation in annealing temperatures, the optimized N/S-CNFs-700 specimen was endowed with dense micro-structure which reduced the contact area of electrolyte/active substance and improved the ICE, along with the more K^+ active sites, enhanced electron/K^+ transport capacity, and enlarged interlayer spacing of carbon layers for efficient potassium storage. DFT calculations indicate that N and S doping significantly improves the K^+ storage performance of N/S-CNFs by enhancing the electric conductivity and improving the adsorption of K^+. Detailed *in-situ* XRD studies reveal the intrinsic electrochemical K^+-storage process. When evaluated as an anode, the resultant N/S-CNF-700 obtained high reversible capacities of ~328.1 mAh g^{-1} at 0.1 A g^{-1} and ~122.0 mAh g^{-1} at 5.0 A g^{-1}, and a high ICE of ~51.5%. When assembled with cognate aPCNF, the constructed PIHCs delivered a large energy density (~106.0 Wh kg^{-1} at 250.0 W kg^{-1}), remarkable cycling stability (the capacity retention of 98.4% after 10,000 consecutive charge-discharge cycles), and small leakage current (~6 μA)/self-discharge capacity (a voltage drop of 0.79 V after 20 h), which is promising for commercial applications. This work inspires future optimization of energy storage materials by structure and doping engineering for PIHCs and beyond.

DECLARATIONS

Authors' contributions

Methodology, formal analysis, investigation, manuscript writing: Sun, J.; Wang, G.
Validation, resources, formal analysis: Wang, G.; Jia, M.; Chen, M.
Methodology, visualization, investigation: Sun, J.; Wang, G.; Yue, P.; Ren, Y.
Project administration, conceptualization, funding acquisition, supervision, manuscript writing: Sun, J.; Ren, Y.; Jiang, H.; Liu, Y.
Project administration, funding acquisition: Hou, L.; Yuan, C.
Project administration, conceptualization, funding acquisition, supervision: Hou, L.; Yuan, C.

Availability of data and materials

The data supporting our work can be found in the Supplementary Materials.

Financial support and sponsorship

This work is supported by the National Natural Science Foundation of China (Nos. U22A20145, 52072151, 52171211, 52271218), Jinan Independent Innovative Team (2020GXRC015), Major Program of Shandong Province Natural Science Foundation (ZR2023ZD43, ZR2021ZD05), and Science and Technology Program of University of Jinan (XKY2119).

Conflicts of interest

All authors declare that there are no conflicts of interest.

Ethical approval and consent to participate

Not applicable.

Consent for publication

Not applicable.

Copyright

REFERENCES

1. Wu, M.; Hu, X.; Zheng, W.; Chen, L.; Zhang, Q. Recent advances in porous carbon nanosheets for high-performance metal-ion capacitors. *Chem. Eng. J.* **2023**, *466*, 143077. DOI
2. Nagamuthu, S.; Zhang, Y.; Xu, Y.; et al. Non-lithium-based metal ion capacitors: recent advances and perspectives. *J. Mater. Chem. A.* **2022**, *10*, 357-78. DOI
3. Xu, Y.; Zhang, C.; Zhou, M.; et al. Highly nitrogen doped carbon nanofibers with superior rate capability and cyclability for potassium ion batteries. *Nat. Commun.* **2018**, *9*, 1720. DOI PubMed PMC
4. Wu, Y.; Sun, Y.; Tong, Y.; et al. Recent advances in potassium-ion hybrid capacitors: electrode materials, storage mechanisms and performance evaluation. *Energy. Storage. Mater.* **2021**, *41*, 108-32. DOI
5. Cheng, L.; Quan, J.; Li, H. Recent advances in antimony-based anode materials for potassium-ion batteries: material selection, structural design and storage mechanisms. *Chinese. Chem. Lett.* **2024**, *36*, 110685. DOI
6. Li, X.; Chen, M.; Wang, L.; et al. Nitrogen-doped carbon nanotubes as an anode for a highly robust potassium-ion hybrid capacitor. *Nanoscale. Horiz.* **2020**, *5*, 1586-95. DOI
7. Jian, Z.; Luo, W.; Ji, X. Carbon electrodes for K-ion batteries. *J. Am. Chem. Soc.* **2015**, *137*, 11566-9. DOI PubMed
8. Cai, P.; Wang, K.; Wang, T.; et al. Comprehensive insights into potassium-ion capacitors: mechanisms, materials, devices and future perspectives. *Adv. Energy. Mater.* **2024**, *14*, 2401183. DOI
9. Ma, J.; Gu, J.; Li, B.; Yang, S. Facile fabrication of 2D stanene nanosheets via a dealloying strategy for potassium storage. *Chem. Commun.* **2019**, *55*, 3983-6. DOI
10. Li, J.; Rui, B.; Wei, W.; et al. Nanosheets assembled layered MoS_2/MXene as high performance anode materials for potassium ion batteries. *J. Power. Sources.* **2020**, *449*, 227481. DOI
11. Chong, S.; Sun, L.; Shu, C.; et al. Chemical bonding boosts nano-rose-like MoS_2 anchored on reduced graphene oxide for superior potassium-ion storage. *Nano. Energy.* **2019**, *63*, 103868. DOI
12. Li, D.; Zhang, Y.; Sun, Q.; et al. Hierarchically porous carbon supported Sn_4P_3 as a superior anode material for potassium-ion batteries. *Energy. Storage. Mater.* **2019**, *23*, 367-74. DOI
13. Dong, S.; Li, Z.; Xing, Z.; Wu, X.; Ji, X.; Zhang, X. Novel potassium-ion hybrid capacitor based on an anode of $K_2Ti_6O_{13}$ microscaffolds. *ACS. Appl. Mater. Interfaces.* **2018**, *10*, 15542-7. DOI
14. Jiang, Y.; Lao, J.; Dai, G.; Ye, Z. Advanced insights on MXenes: categories, properties, synthesis, and applications in alkali metal ion batteries. *ACS. Nano.* **2024**, *18*, 14050-84. DOI
15. Lu, C.; Sun, Z.; Yu, L.; et al. Enhanced kinetics harvested in heteroatom dual-doped graphitic hollow architectures toward high rate printable potassium□ion batteries. *Adv. Energy. Mater.* **2020**, *10*, 2001161. DOI
16. Liu, Y.; Lu, Y. X.; Xu, Y. S.; et al. Pitch-derived soft carbon as stable anode material for potassium ion batteries. *Adv. Mater.* **2020**, *32*, e2000505. DOI
17. Li, C.; Zhang, X.; Lv, Z.; et al. Scalable combustion synthesis of graphene-welded activated carbon for high-performance supercapacitors. *Chem. Eng. J.* **2021**, *414*, 128781. DOI
18. Xu, Z.; Wu, M.; Chen, Z.; et al. Direct structure-performance comparison of all-carbon potassium and sodium ion capacitors. *Adv. Sci.* **2019**, *6*, 1802272. DOI
19. Li, Z.; Shin, W.; Chen, Y.; Neuefeind, J. C.; Greaney, P. A.; Ji, X. Low temperature pyrolyzed soft carbon as high capacity K-ion anode. *ACS. Appl. Energy. Mater.* **2019**, *2*, 4053-8. DOI
20. Liu, Q.; Han, F.; Zhou, J.; et al. Boosting the potassium-ion storage performance in soft carbon anodes by the synergistic effect of optimized molten salt medium and N/S dual-doping. *ACS. Appl. Mater. Interfaces.* **2020**, *12*, 20838-48. DOI
21. Bi, H.; He, X.; Yang, L.; Li, H.; Jin, B.; Qiu, J. Interconnected carbon nanocapsules with high N/S co-doping as stable and high-capacity potassium-ion battery anode. *J. Energy. Chem.* **2022**, *66*, 195-204. DOI
22. Ruan, J.; Wu, X.; Wang, Y.; et al. Nitrogen-doped hollow carbon nanospheres towards the application of potassium ion storage. *J. Mater. Chem. A.* **2019**, *7*, 19305-15. DOI

23. Luo, H.; Chen, M.; Cao, J.; et al. Cocoon silk-derived, hierarchically porous carbon as anode for highly robust potassium-ion hybrid capacitors. *Nanomicro. Lett.* **2020**, *12*, 113. DOI PubMed PMC
24. Poudel, M. B.; Kim, A. R.; Ramakrishan, S.; et al. Integrating the essence of metal organic framework-derived ZnCoTe-N-C/MoS_2 cathode and ZnCo-NPS-N-CNT as anode for high-energy density hybrid supercapacitors. *Compos. Part. B. Eng.* **2022**, *247*, 110339. DOI
25. Li, X.; Sun, N.; Tian, X.; et al. Electrospun coal liquefaction residues/polyacrylonitrile composite carbon nanofiber nonwoven fabrics as high-performance electrodes for lithium/potassium batteries. *Energy. Fuels.* **2020**, *34*, 2445-51. DOI
26. Zhang, Y.; Wang, G.; Yue, P.; et al. Construction of low-softening-point coal pitch derived carbon nanofiber films as self-standing anodes toward sodium dual-ion batteries. *Adv. Funct. Mater.* **2025**, *35*, 2414761. DOI
27. Wang, G.; Wang, X.; Sun, J.; Zhang, Y.; Hou, L.; Yuan, C. Porous carbon nanofibers derived from low-softening-point coal pitch towards all-carbon potassium ion hybrid capacitors. *Rare. Met.* **2022**, *41*, 3706-16. DOI
28. Wang, B.; Zhang, Z.; Yuan, F.; et al. An insight into the initial coulombic efficiency of carbon-based anode materials for potassium-ion batteries. *Chem. Eng. J.* **2022**, *428*, 131093. DOI
29. Ramakrishnan, S.; Karuppannan, M.; Vinothkannan, M.; Ramachandran, K.; Kwon, O. J.; Yoo, D. J. Ultrafine Pt nanoparticles stabilized by MoS_2/N-doped reduced graphene oxide as a durable electrocatalyst for alcohol oxidation and oxygen reduction reactions. *ACS. Appl. Mater. Interfaces.* **2019**, *11*, 12504-15. DOI
30. Zhang, W.; Liu, Y.; Guo, Z. Approaching high-performance potassium-ion batteries via advanced design strategies and engineering. *Sci. Adv.* **2019**, *5*, eaav7412. DOI PubMed PMC
31. Tao, L.; Yang, Y.; Wang, H.; et al. Sulfur-nitrogen rich carbon as stable high capacity potassium ion battery anode: Performance and storage mechanisms. *Energy. Storage. Mater.* **2020**, *27*, 212-25. DOI
32. Cheng, C.; Wu, D.; Gong, T.; et al. Internal and external cultivation design of zero-strain columbite-structured MNb_2O_6 toward lithium-ion capacitors as competitive anodes. *Adv. Energy. Mater.* **2023**, *13*, 2302107. DOI
33. Xu, K.; Ding, S. P.; Jow, T. R. Toward reliable values of electrochemical stability limits for electrolytes. *J. Electrochem. Soc.* **1999**, *146*, 4172-8. DOI
34. Yao, Y.; Xu, R.; Chen, M.; et al. Encapsulation of SeS_2 into nitrogen-doped free-standing carbon nanofiber film enabling long cycle life and high energy density K-SeS_2 battery. *ACS. Nano.* **2019**, *13*, 4695-704. DOI
35. Shen, Y.; Huang, C.; Li, Y.; et al. Enhanced sodium and potassium ions storage of soft carbon by a S/O co-doped strategy. *Electrochim. Acta.* **2021**, *367*, 137526. DOI
36. Wang, C.; Yang, D.; Zhang, W.; Qin, Y.; Qiu, X.; Li, Z. Engineering of edge nitrogen dopant in carbon nanosheet framework for fast and stable potassium-ion storage. *Carbon. Res.* **2024**, *3*, 20. DOI
37. Wei, X.; Yi, Y.; Yuan, X.; et al. Intrinsic carbon structure modification overcomes the challenge of potassium bond chemistry. *Energy. Environ. Sci.* **2024**, *17*, 2968-3003. DOI
38. Hou, L.; Chen, Z.; Zhao, Z.; Sun, X.; Zhang, J.; Yuan, C. Universal $FeCl_3$-activating strategy for green and scalable fabrication of sustainable biomass-derived hierarchical porous nitrogen-doped carbons for electrochemical supercapacitors. *ACS. Appl. Energy. Mater.* **2019**, *2*, 548-57. DOI
39. Huang, R.; Zhang, X.; Qu, Z.; et al. Defects and sulfur-doping design of porous carbon spheres for high-capacity potassium-ion storage. *J. Mater. Chem. A.* **2022**, *10*, 682-9. DOI
40. Duan, M.; Zhu, F.; Zhao, G.; et al. Nitrogen and sulfur co-doped mesoporous carbon derived from ionic liquid as high-performance anode material for sodium ion batteries. *Microporous. Mesoporous. Mater.* **2020**, *306*, 110433. DOI
41. Xie, Z.; Xia, J.; Qiu, D.; et al. Rich-phosphorus/nitrogen co-doped carbon for boosting the kinetics of potassium-ion hybrid capacitors. *Sustain. Energy. Fuels.* **2021**, *6*, 162-9. DOI
42. Yin, R.; Wang, K.; Han, B.; et al. Structural evaluation of coal-tar-pitch-based carbon materials and their Na^+ storage properties. *Coatings* **2021**, *11*, 948. DOI
43. Liu, Y.; Wang, S.; Sun, X.; et al. Sub-nanoscale engineering of MoO_2 clusters for enhanced sodium storage. *Energy. Environ. Mater.* **2023**, *6*, e12263. DOI
44. Zhao, J.; Yang, S.; Zhang, P.; Dai, S. Sulphur as medium: directly converting pitch into porous carbon. *Fuel* **2021**, *286*, 119393. DOI
45. Cai, P.; Momen, R.; Tian, Y.; et al. Advanced pre-diagnosis method of biomass intermediates toward high energy dual-carbon potassium-ion capacitor. *Adv. Energy. Mater.* **2022**, *12*, 2103221. DOI
46. Hu, X.; Liu, Y.; Chen, J.; Yi, L.; Zhan, H.; Wen, Z. Fast redox kinetics in Bi-heteroatom doped 3D porous carbon nanosheets for high-performance hybrid potassium-ion battery capacitors. *Adv. Energy. Mater.* **2019**, *9*, 1901533. DOI
47. Lotfabad E, Kalisvaart P, Kohandehghan A, Karpuzov D, Mitlin D. Origin of non-SEI related coulombic efficiency loss in carbons tested against Na and Li. *J. Mater. Chem. A.* **2014**, *2*, 19685-95. DOI
48. Ning, G.; Ma, X.; Zhu, X.; et al. Enhancing the Li storage capacity and initial coulombic efficiency for porous carbons by sulfur doping. *ACS. Appl. Mater. Interfaces.* **2014**, *6*, 15950-8. DOI
49. Tang, H.; Yan, D.; Lu, T.; Pan, L. Sulfur-doped carbon spheres with hierarchical micro/mesopores as anode materials for sodium-ion batteries. *Electrochim. Acta.* **2017**, *241*, 63-72. DOI
50. Xiao, N.; Zhang, X.; Liu, C.; Wang, Y.; Li, H.; Qiu, J. Coal-based carbon anodes for high-performance potassium-ion batteries. *Carbon* **2019**, *147*, 574-81. DOI
51. Li, Q.; Wang, T.; Shu, T.; et al. Controllable construction of hierarchically porous carbon composite of nanosheet network for

advanced dual-carbon potassium-ion capacitors. *J. Colloid. Interface. Sci.* **2022**, *621*, 169-79. DOI

52. Zeng, S.; Zhou, X.; Wang, B.; et al. Freestanding CNT-modified graphitic carbon foam as a flexible anode for potassium ion batteries. *J. Mater. Chem. A.* **2019**, *7*, 15774-81. DOI
53. Liu, C.; Zheng, H.; Yu, K.; et al. Direct synthesis of P/O-enriched pitch-based carbon microspheres from a coordinated emulsification and pre-oxidation towards high-rate potassium-ion batteries. *Carbon* **2022**, *194*, 176-84. DOI
54. Xu, J.; Dou, S.; Zhou, W.; et al. Scalable waste-plastic-derived carbon nanosheets with high contents of inbuilt nitrogen/sulfur sites for high performance potassium-ion hybrid capacitors. *Nano. Energy.* **2022**, *95*, 107015. DOI
55. Wang, M.; Zhu, Y.; Zhang, Y.; et al. Isotropic high softening point petroleum pitch-based carbon as anode for high-performance potassium-ion batteries. *J. Power. Sources.* **2021**, *481*, 228902. DOI
56. Shen, C.; Yuan, K.; Tian, T.; et al. Flexible sub-micro carbon fiber@CNTs as anodes for potassium-ion batteries. *ACS. Appl. Mater. Interfaces.* **2019**, *11*, 5015-21. DOI
57. Sun, Y.; Wang, H.; Wei, W.; et al. Sulfur-rich graphene nanoboxes with ultra-high potassiation capacity at fast charge: storage mechanisms and device performance. *ACS. Nano.* **2021**, *15*, 1652-65. DOI
58. Zhang, C.; Han, F.; Wang, F.; et al. Improving compactness and reaction kinetics of MoS_2@C anodes by introducing Fe_9S_10 core for superior volumetric sodium/potassium storage. *Energy. Storage. Mater.* **2020**, *24*, 208-19. DOI
59. Huang, N.; Tang, C.; Jiang, H.; Sun, J.; Du, A.; Zhang, H. Interfacial growth of N,S-codoped mesoporous carbon onto biomass-derived carbon for superior potassium-ion storage. *Nano. Res.* **2024**, *17*, 2619-27. DOI
60. Yang, W.; Zhou, J.; Wang, S.; et al. A three-dimensional carbon framework constructed by N/S Co-doped graphene nanosheets with expanded interlayer spacing facilitates potassium ion storage. *ACS. Energy. Lett.* **2020**, *5*, 1653-61. DOI
61. Lv, C.; Xu, W.; Liu, H.; et al. 3D sulfur and nitrogen codoped carbon nanofiber aerogels with optimized electronic structure and enlarged interlayer spacing boost potassium-ion storage. *Small* **2019**, *15*, e1900816. DOI
62. Sun, X.; Zhang, X.; Wang, K.; et al. Determination strategy of stable electrochemical operating voltage window for practical lithium-ion capacitors. *Electrochim. Acta.* **2022**, *428*, 140972. DOI
63. Gao, Q.; Li, T.; Liu, C.; et al. Hierarchically porous N-doped carbon framework with enlarged interlayer spacing as dual-carbon electrodes for potassium ion hybrid capacitors. *Carb. Neutral.* **2023**, *2*, 57. DOI
64. Qiu, D.; Guan, J.; Li, M.; et al. Kinetics enhanced nitrogen-doped hierarchical porous hollow carbon spheres boosting advanced potassium-ion hybrid capacitors. *Adv. Funct. Mater.* **2019**, *29*, 1903496. DOI
65. Cao, J.; Xu, H.; Zhong, J.; et al. Dual-carbon electrode-based high-energy-density potassium-ion hybrid capacitor. *ACS. Appl. Mater. Interfaces.* **2021**, *13*, 8497-506. DOI
66. Fan, L.; Lin, K.; Wang, J.; Ma, R.; Lu, B. A nonaqueous potassium-based battery-supercapacitor hybrid device. *Adv. Mater.* **2018**, *30*, e1800804. DOI
67. Luo, Y.; Liu, L.; Lei, K.; et al. A nonaqueous potassium-ion hybrid capacitor enabled by two-dimensional diffusion pathways of dipotassium terephthalate. *Chem. Sci.* **2019**, *10*, 2048-52. DOI
68. Zhao, S.; Yan, K.; Liang, J.; et al. Phosphorus and oxygen dual-doped porous carbon spheres with enhanced reaction kinetics as anode materials for high-performance potassium-ion hybrid capacitors. *Adv. Funct. Mater.* **2021**, *31*, 2102060. DOI
69. Zhang, H.; Fang, L.; Guo, Y.; et al. Nitrogen-sulfur co-doped ZIF-8-derived carbon materials for supercapacitors with low self-discharge. *J. Energy. Storage.* **2024**, *80*, 110138. DOI